RSC Advances

ROYAL SOCIETY OF CHEMISTRY

www.rsc.org/advances

Journal Name

ARTICLE

Synthesis of ultrafine amorphous PtP nanoparticles and the effect of PtP crystallinity on methanol oxidation

Yanjiao Ma,[a] Hui Wang,[a] Hao Li,[b] Julian Key[c], Shan Ji,** [c] and Rongfang Wang,*[a]

In this study we report that ultrafine amorphous metallic nanoparticles have a surface structure that is both rich in low-coordination sites and defects that coincides with increased methanol oxidation activity. Ultrafine amorphous platinum-phosphorous nanoparticles supported on Vulcan carbon (PtP$_a$/C) were synthesized, followed by increasing degrees of heat treatment to obtain higher levels of crystallinity in the supported PtP particles. Structural and compositional analysis by various techniques allowed correlation between the structures of various PtP states and their resultant catalytic methanol oxidation activity. Increasing heat treatment temperature increased both the crystallinity and average size of the supported PtP particles. Both factors coincided with decreased methanol oxidation activity and lower carbon monoxide tolerance. The most amorphous PtP nanoparticles had the highest catalytic methanol oxidation activity and strongest tolerance for carbon monoxide.

Introduction

Pt and Pt-based nanoparticles deposited on carbon supports dominate as anode catalysts for direct methanol fuel cells (DMFC) due to their high specific surface area, high mass activity and stability.[1,2] However, the prohibitive cost, scarcity and eventual activity decay of Pt-based catalysts prevents the widespread use and commercialization of fuel cells. To overcome these issues requires a significant increase in the mass activity of Pt-based catalysts. Engineering of catalyst morphology and composition to reduce the usage of Pt offers a promising approach.

It is well-known that electrocatalytic performance (including activity, selectivity, and stability) can be improved by altering catalyst morphology,[3,4] particle size,[5,6] surface composition and structure.[7,8] These factors strongly relate to the surface atomic arrangement and configurations associated with terraces, steps, kinks, and vacancies, which act as active sites in catalytic reactions.[9,10] Amorphous alloy nanoparticles constitute an overlapping region of two active fields by combining the unique properties together, i.e., long-range disorder with short-range order in structure, and the striking characteristics of nano-sized material.[11-13] The surface of amorphous material is rich in low-coordination sites (terraces, steps, corner atoms) and defects.[14,15] It was well-documented that the low-coordination sites play important roles in catalysis. A number of papers report the synthesis of amorphous alloy nanoparticles, such as, CoB,[16] FeB,[17] NiMoB,[18] FeNiPt,[12] which exhibit good catalytic activity due to their unique structural properties. However, since the average particle size of these amorphous powders prepared by ball milling is large, their relatively small surface area limits their electrocatalytic activity.

Pt-based amorphous nanoparticles synthesized by chemical methods have rarely been explored for fuel cell electrocatalysts and offer an interesting avenue to obtain further improvement of Pt mass activity. Moreover, synthesis of nano-sized electrocatalyst in the desired ultrafine size range is an effective approach to improve the mass activity. Phosphorus, with its abundant valence electrons, when incorporated into the catalyst has significant effects on both magnetic and catalytic activity, resulting in ultrafine particles size.[19-21]

In this study, we developed a method to synthesize carbon-supported ultrafine PtP nanoparticles with amorphous structure. The catalyst's morphology and electrocatalytic properties were investigated and compared to those of its crystalline counterparts prepared at various heat-treatment temperatures.

Experimental

Preparation of PtP/C catalysts

Amorphous PtP nanoparticles supported on carbon were prepared by reducing its precursors in aqueous solution using NaBH$_4$. The detailed procedure is as follows: 9.96 mL H$_2$PtCl$_6$ (20 mg mL^{-1}) and 300 mg NaH$_2$PO$_2$•H$_2$O were dissolved in aqueous solution and stirred for 0.5 h. The solution was adjusted to ~ pH 8.0 through addition of 3 mol L^{-1} NaOH solution with vigorous stirring. The pretreated carbon black Vulcan® XC72R (300 mg) was added to the above mixture with stirring. 20 mL NaBH$_4$ aqueous solution (0.2 mol L^{-1}) was then slowly added to the mixture and allowed to react for 12 h. The resultant product, PtP$_a$/C, was collected by filtration, and then washed with deionized water several times and finally dried in an oven at 50 ºC for 8 h.

Crystalline PtP/C counterparts of the above catalyst were obtained via heating in a tube furnace under N$_2$ atmosphere at various

temperatures for 2 h. The resultant PtP/C catalysts heated at 200, 300 and 400 ºC are denoted as PtP-200/C, PtP-300/C and PtP-400/C, respectively.

Characterization

X-ray diffraction (XRD) patterns of the catalysts were recorded on a Shimadzu XD–3A (Japan) using filtered Cu-Kα radiation generated at 40 kV and 30 mA. Transmission electron micrographs (TEM), high angle annular dark field scanning transmission electron microscopy (HAADF-STEM) images of the catalysts were taken on a JEOL (JEM-2000 FX) microscope operating at 200 kV. Energy dispersive spectroscopy (EDS) in the STEM mode was employed for elemental composition using either individual particles or several particles. X-ray photoelectron spectra (XPS) were recorded using a VG Escalab210 spectrometer fitted with Mg 300 W X-ray source.

Measurements

Electrochemical measurements of catalysts were performed using an electrochemical work station (CHI 650D). A common three-electrode electrochemical cell was used for the measurements. The cell comprised a platinum wire counter electrode, an Ag/AgCl (3 mol L^{-1} KCl) reference electrode, and a thin-film working electrode mounted on a glassy carbon disk of 5 mm in diameter. The thin-film electrode was prepared as follows: 5 mg of catalyst was dispersed ultrasonically in 1 mL Nafion/ethanol (0.25% Nafion) for 15 min. 8 μL of the dispersion was transferred on to the glassy carbon disk and then dried in air. Stable cyclic voltammograms (CVs) were recorded after 24 cycles. For CO stripping tests, CO was adsorbed on the working electrode by bubbling CO through the cell for 5 min, which was followed by transferring the working electrode to another cell containing 0.5 mol L^{-1} H_2SO_4 solution purged with nitrogen.
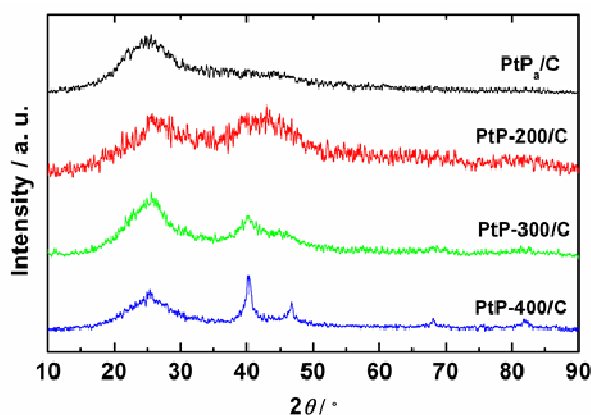
Results and discussion

Fig. 1 The XRD patterns of the four PtP/C catalysts.

Fig. 1 shows the XRD patterns of the PtP_a/C catalyst and its heat treated crystalline counterparts. All the catalysts produced a diffraction peak at ~25° corresponding to the (200) reflection of the hexagonal structure of Vulcan carbon.[22] Unlike its crystalline counterparts, PtP_a/C produced no additional peaks, suggesting that its structure was both amorphous and nanoparticulate.[23-25] With 200 ºC heat treatment, the PtP-200/C catalyst produced a broad peak at the 2θ range from 36º to 51º, with no sharp peaks relating to a periodic lattice; this suggests amorphous structure was retained but with an increase particle size. PtP-300/C produced a peak at ca. $2\theta \approx$

40° correlating to the (111) reflection of face-centered cubic (fcc) Pt (JCPDS, No. 04-0802), and a weak peak between 43.5 and 48.8° which due to their undefined position did not confirm a periodic lattice. These results indicate that PtP nanoparticles started to crystallize at 300 ºC.[26] PtP-400/C produced several sharp diffraction peaks, indicating it changed from an amorphous to crystalline state. The diffraction peaks at 40.3°, 46.8°, 68.2°, and 82.0° correlate to the (111), (200), (220), and (300) reflections of fcc Pt respectively. The peaks of PtP-400 nanoparticles shift to a higher angle compared to that of pure fcc Pt, which was likely due to lattice contraction caused by incorporation of P atoms.[27] The XRD results show that at high temperatures the structure of PtP nanoparticles changes from amorphous to crystalline.
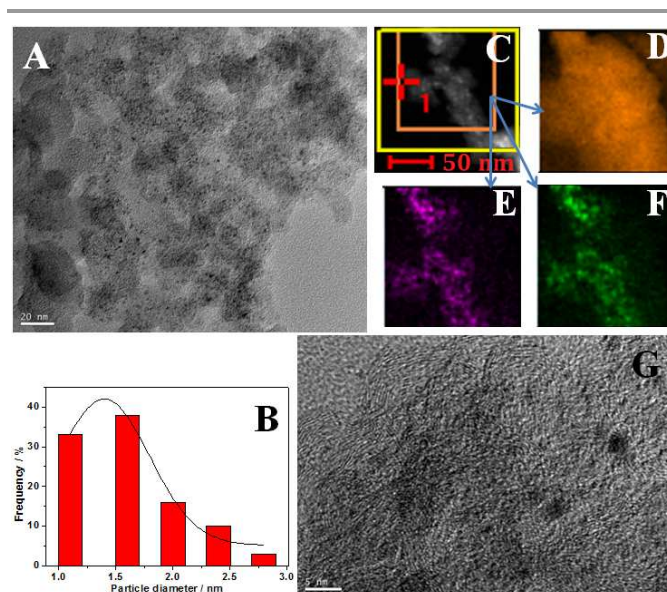

Fig. 2 (A) TEM image of PtP_a/C catalyst; (B) the particle size distribution of PtP_a/C catalyst; (C) HAADF-STEM characterization of PtP_a/C catalyst, and the elemental mapping of C (D), Pt (E), and P (F); (G) HRTEM image of PtP_a/C catalyst.

The TEM image of PtP_a/C (Fig. 2A) shows ultrafine PtP_a nanoparticles were uniformly distributed on the carbon surface. The particle size of PtP_a nanoparticles (Fig. 2B) ranged from ~1.0 to 2.8 nm at an average of ca. 1.4 nm. The chemical microstructure of PtP_a nanoparticles was examined using electron energy loss spectroscopic (EELs) mapping. Fig. 2c shows the HAADF-STEM image of PtP_a/C where the area circled by orange box was spectroscopically imaged. Fig. 2D-F shows the distribution of C, Pt and P elements in the catalyst respectively. Overlapping positions of the Pt (purple, Fig. 2E) and P (blue, Fig. 2F) particles indicates formation of PtP alloy structure. The high resolution TEM (HRTEM) image of PtP_a/C (Fig. 2G) shows dark spots of PtP_a nanoparticles against the lighter carbon background. The lack of lattice fringes in PtP_a nanoparticles indicates the amorphous state of PtP_a nanoparticles.[28] The elemental composition of PtP_a/C analyzed by EDS shows the amounts of Pt, P and C in PtP_a/C were 22.2 wt%, 1.8 wt%, and 76.0 wt% respectively.

Fig. 3 shows the TEM images of PtP-200/C, PtP-300/C and PtP-400/C. Fig. 3A shows PtP-200 nanoparticles were well dispersed on the carbon surface with uniform particle size distribution at an average of ca. 1.6 nm. Heat-treatment at
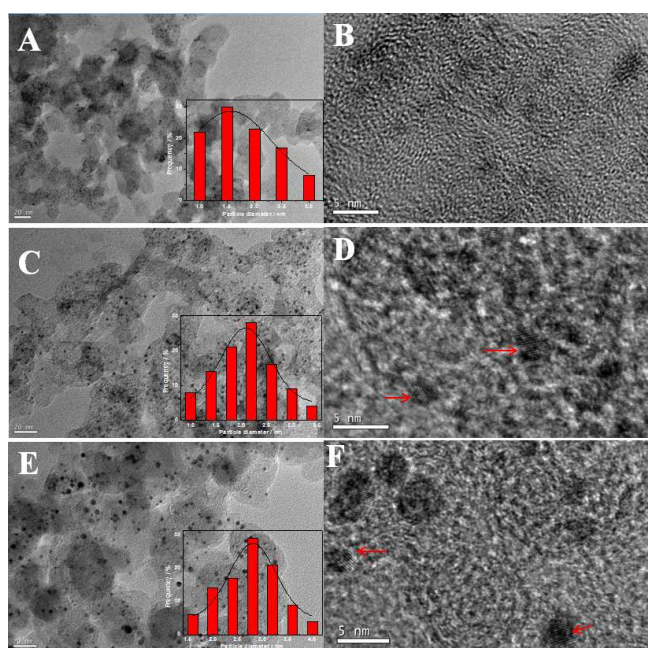
Fig. 3 (A, C, and E) TEM images and (B, D, and F) HRTEM of PtP-200/C, PtP-300/C, and PtP-400/C catalysts respectively; Inset: the corresponding particle size distribution histograms

Table 1. Assignments, binding energies and concentrations of Pt 4f species in the catalysts obtained from XPS results

Catalyst	Pt:P[a]	Pt 4f$_{7/2}$	BE[b]	Concentration[c]
PtP$_a$/C	1.6:1.0	0	72.4	0.05
		2	73.3	0.68
		4	74.9	0.27
PtP-200/C	1.6:1.0	0	72.0	0.07
		2	72.9	0.75
		4	74.4	0.18
PtP-300/C	1.7:1.0	0	71.9	0.14
		2	72.7	0.62
		4	74.3	0.24
PtP-400/C	1.0:1.0	0	71.9	0.37
		2	72.7	0.37
		4	74.3	0.26

[a] Atomic ratio. [b] Binding energy (eV). [c] Per species.

200 °C did not result in the agglomeration of PtP nanoparticles, which may be attributed to the presence of P.[29] In Fig. 3B, the absence of particles with crystalline fringes indicates that PtP-200 retained amorphous structure. At 300 °C heat-treatment (Fig. 3C), the dispersion of the PtP nanoparticles on carbon was still quite uniform, and ranged from 1.0 to 3.5 nm with average size of 2.1 nm (31 % larger than PtP-200 nanoparticles). In addition, the lattice fringes of Pt nanoparticles became visible for some nanoparticles (as indicated by the red arrows) showing crystalline structure was formed. Similarly, at 400 °C (Fig. 3E) PtP nanoparticles had uniform particle size distribution with an increased average particle size of ca. 2.8 nm (30% larger than PtP-300 nanoparticles). The TEM results show that heat treatment did not affect the uniformity of PtP particle size distribution, but both crystallinity and the average particle size clearly increased with heat treatment from 200 to 400 °C.
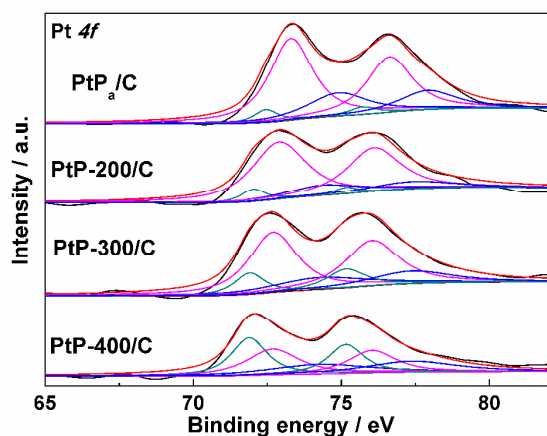
XPS results provided characterization of the surface composition and the valence state of the elements in the catalysts. By estimating the peak areas of the corresponding lines in the original spectra, the surface compositions of the four catalysts were calculated (Table 1). While the atomic ratio of Pt:P doesn't obviously change from PtP$_a$/C to PtP-300/C, the ratio decreases in PtP-400/C. Fig. 4 shows the high resolution Pt 4f XPS spectra of the four catalysts, where two peaks in the Pt 4f XPS spectra correlate to Pt 4f$_{7/2}$ and Pt 4f$_{5/2}$ states due to spin-orbital splitting, which originates from lower energy (Pt 4f$_{7/2}$) and higher-energy (Pt 4f$_{5/2}$) bands. The binding energies (BE) of Pt 4f for the four catalysts shift positively in comparison to that of Pt/C catalyst reported in our previous work[22]. This is likely due to Pt donation of electrons to P. Similar positive shifts were observed on PdP by another group[30]. The electron transfer from Pt to P results in decrease of Pt 4f electron density. Pt atoms with low 4f electron density do not easily bond with intermediates such as CO$_{ads}$, which results in low surface CO$_{ads}$ coverage. Therefore, this would facilitate the methanol oxidation reaction (MOR) on Pt atoms. Furthermore, the BEs of Pt 4f XPS shift negatively from PtP$_a$/C to PtP-400/C, suggesting that the 4f electron density of Pt increases from PtP$_a$/C to PtP-400/C. Therefore, intermediates are more likely to be absorbed on PtP nanoparticles thermally treated at high temperature and MOR activity would foreseeably decrease.

To identify different chemical states of Pt on the surface of the samples, the spectrum of Pt 4f XPS can be fitted by three pairs of overlapping Lorentzian curves (Table 1). Pt in the all catalysts existed predominately in oxidized states, and the percentage of Pt (0) increased from PtP$_a$/C to PtP-400/C, perhaps due to the reduction Pt.

Fig. 5 shows the P 2p XPS spectra of the four catalysts. The P 2p peak shifted positively from PtP$_a$/C to PtP-400/C. Therefore, combined with the negative shifts of Pt 4f XPS from PtP$_a$/C to PtP-400/C, it can be concluded that the electron effect between Pt and P becomes progressively weaker from PtP$_a$/C to PtP-400/C. On the other hand, the P 2p peak can be fitted into two individual component peaks at ~133.4-133.6 eV and 134.4-134.8 (BEs) correlating to P(Ⅲ)[31] and P(Ⅴ)[32,33] respectively. Table 2 shows the BEs relative atomic concentrations of different P species, determined from the peak areas of the all P species. As can be seen in Fig. 5 and Table 2, P element in the
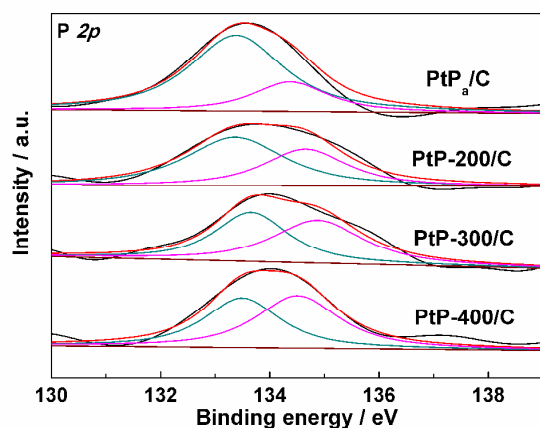

Fig. 4 The Pt 4f spectra of the four PtP/C catalysts.

Fig. 5 The P 2p XPS spectra of the four catalysts.

Table 2. Assignments, binding energies (BEs) and concentrations of P 2p species in various catalysts obtained from XPS results

Catalyst	P 2p	BE[a]	Concentration[b]
PtP$_a$/C	5	134.4	0.24
	3	133.4	0.76
PtP-200/C	5	134.6	0.39
	3	133.4	0.61
PtP-300/C	5	134.8	0.52
	3	133.6	0.48
PtP-400/C	5	134.5	0.54
	3	133.5	0.46

[a] Binding energy (in eV). [b] Per species.

surface was mainly in the oxidized state. The relative amount of P(III) decreased from 76 % in PtP$_a$/C to 46 % in PtP-400/C, which may originate from the change of interaction between P and Pt along with the increase of heat-treatment temperatures.
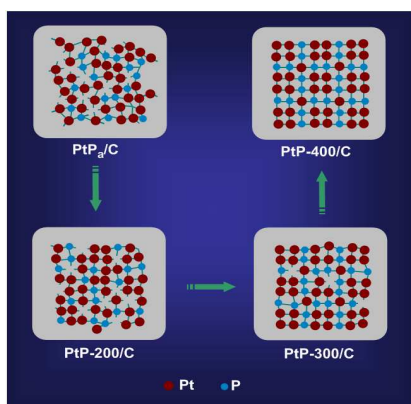

Fig. 6 Schematic illustration showing evolution of PtP nanoparticle structure with progressively higher heat-treatment temperatures.

Fig. 6 illustrates the structural and compositional evolution of PtP nanoparticles with the heat-treatment temperatures. PtP$_a$ nanoparticles had long-range disorder and short-range order as their main structural feature.[34] After PtP$_a$/C was heat-treated at 200 °C, amorphous phase was retained, but with less point defects and less dislocation within the grains resulting in grain boundary zones of medium-range disorder, i.e. the order range became longer[35] on atom rearrangement. Similar change in order range has been observed by Carlo and Alfredo in amorphous GeSe$_2$[36]. With increasing temperature, the order range increased from medium-range order (nanocrystalline phase) of PtP-300/C to long-range order (crystalline structure) of PtP-400/C.
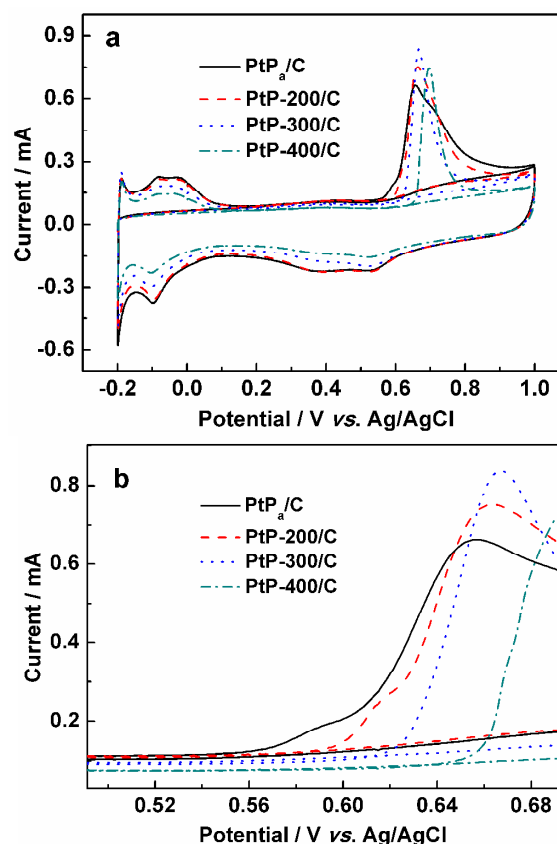

Fig. 7 (a) The CO stripping voltammetries of the four catalysts measured in a nitrogen-saturated 0.5 mol L^{-1} H$_2$SO$_4$ solution; (b) the enlarged CO oxidation region.

Fig. 7 shows the CO stripping voltagrams of the four catalysts measured in nitrogen-saturated 0.5 mol L^{-1} H$_2$SO$_4$ solution. In Fig. 7a, hydrogen desorption peaks were completely suppressed in the lower potential region (-0.2 to 0.1 V) on the forward scan of the first scan. This was due to saturated coverage of CO$_{ads}$ species on the surface of nanoparticle active sites,[37] following a peak at higher potential, between 0.6 and 1.0 V corresponding to CO oxidation. On the reverse sweep, the defined peak near 0.55 V is characteristic of oxide reduction, and after that, the hydrogen adsorption peak appears because the active sites are freed after the CO is removed by oxidation. On the forward scan of the second cycle, the characteristic features of hydrogen desorption peak ranged from 0.1 to -0.2 V.

To more clearly observe the CO oxidation onset potentials of the four catalysts, the range between 0.49 and 0.69 V is enlarged in Fig. 7b. The onset potential clearly follows the order: $PtP_a/C <$ PtP-200/C $<$ PtP-300/C $<$ PtP-400/C. As discussed above, the 4f electron density of Pt atoms increases from PtP_a/C to PtP-400/C, and the adsorption energy toward CO on the Pt active site becomes progressively stronger from PtP_a/C to PtP-400/C, making CO oxidation progressively difficult. PtP_a/C has the most negative onset potential of CO oxidation.[38] In addition, shift in the onset potential of the catalysts' oxidation peaks followed the same trend as the shifts in CO stripping onset potential.
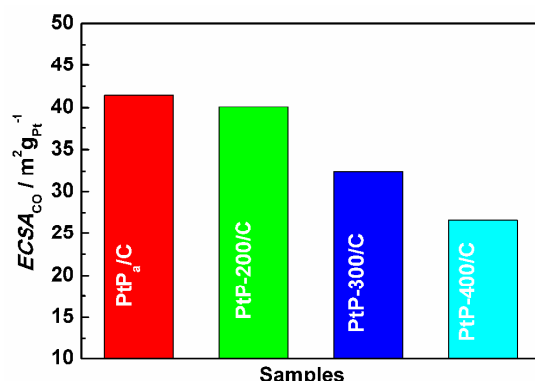

Fig. 8 The diagram of $ECSA_{CO}$ of the four catalysts.

The electrochemical surface area ($ECSA$) is an important factor for the reactions in fuel cells, and the utilization ratio of electrocatalyst is closely interrelated with the $ECSA$. The $ECSA$s of different catalysts were calculated according to the equation (1):[39,40]

$$ECSA_{CO} = \frac{Q_{CO}}{K\omega} \quad (1)$$

where Q_{CO} (C m^{-2}) is the average integrated charge in the CO oxidation peak area in the CV curves after subtracting the charge from the double-layer region, ω is the Pt loading on the electrode, and K is 4.2, the charge (C m^{-2}) required to oxidize a monolayer of carbon monoxide on the precious metal surface, respectively. The estimated $ECSA_{CO}$ of the catalysts (Fig. 8) shows PtP_a/C had largest $ECSA_{CO}$.

Fig. 9 shows the methanol oxidation activities of the four PtP/C catalysts evaluated by cyclic voltammetry (CV). The current was normalized to Pt loading and $ECSA_{CO}$. Fig. 9a shows the current densities of the oxidation peaks on the four catalysts follow the order $PtP_a/C >$ PtP-200/C $>$ PtP-300/C $>$ PtP-400/C. The onset potentials of methanol oxidation (Fig. 9b) followed the trend of: $PtP_a/C \sim$ PtP-200/C $<$ PtP-300/C $\sim$ PtP-400/C. Fig. 9c shows a similar trend to that of Fig. 9a, which indicates the specific activity of PtP_a/C is higher than other catalysts. PtP_a/C produced the highest methanol oxidation current, and had the most negative onset potential for methanol oxidation, and was therefore the most effective of the four catalysts[41].

The question of why PtP_a/C had the highest catalytic activity is interesting. TEM showed that nanoparticle size increased from PtP-200 to PtP-400, which could result in lower catalytic activity due to less active surface sites as demonstrated by $ECSA_{CO}$. However, increase of average particle size from PtP_a/C to PtP-200/C, was only very small, ca. 0.2 nm, and the

$ECSA_{CO}$ of the two catalysts was almost same, suggesting that the amount of the electrochemical active sites from Pt atoms was similar. Therefore, a reason other than particle size would appear to account for the difference in activity between PtP_a/C and PtP-200/C. This point is considered below.
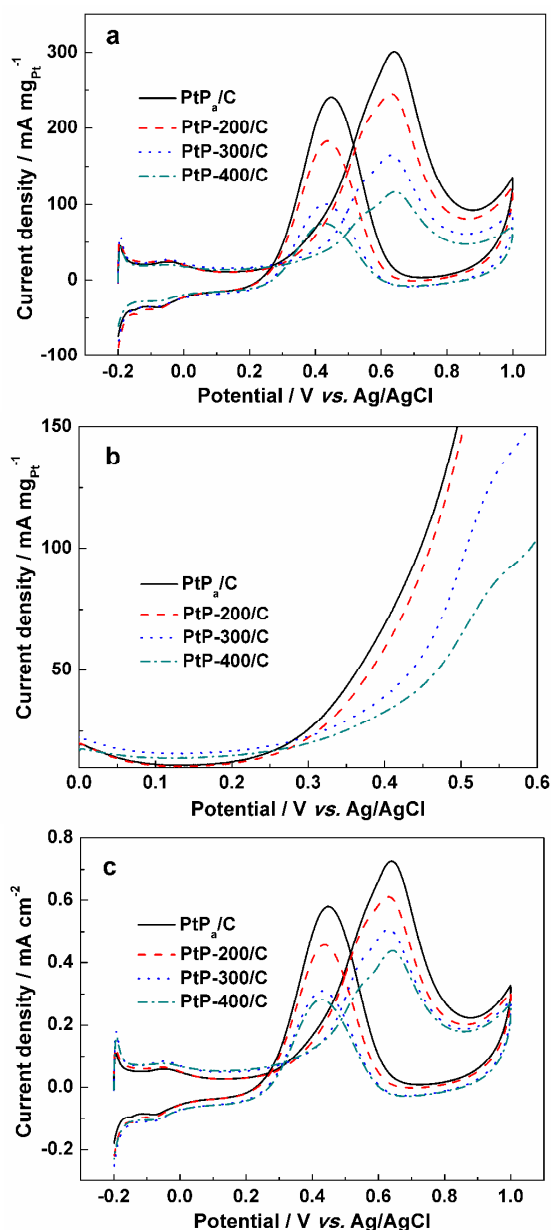

Fig. 9 (a) CVs normalized by the Pt loading of the four catalysts obtained at 50 mV s^{-1} in 0.5 mol L^{-1} H$_2$SO$_4$ + 0.5 mol L^{-1} CH$_3$OH solution; (b) the enlarged methanol oxidation range derived from Figure a; (c) CVs normalized by $ECSA_{CO}$ for the four catalysts obtained at 50 mV s^{-1} in 0.5 mol L^{-1} H$_2$SO4 + 0.5 mol L^{-1} CH$_3$OH solution.

Conventional active sites are considered to exist on the surface of metal particles,[42] and Maillard et al.[43] have proposed that the grain boundary between small crystals act as the active sites. Recently, Kang et al. identified the active sites for carbon monoxide oxidation on Au-FeO$_x$ catalysts by using Au-FeO$_x$ binary super lattices correlating the activity to the number density of catalytic contacts between Au and FeO$_x$.[44] They also

demonstrated that the active sites for oxygen reduction on Pt-Pd binary catalyst include the contacts between Pt and Pd.[45] From the results of these papers, we infer that the defect points on the PtP_a surface may act as the active sites. After PtP_a/C was heat-treated at 200 °C, the number of the defect points decreased, resulting in less active sites, corresponding to lower catalytic activity. To confirm this hypothesis, PtP-100/C was prepared and its electrochemical performance tested. Fig.S1-3 (Supporting Information) shows, as predicted, the catalytic activity of PtP-100/C was lower than that of PtP_a/C, but higher than that of PtP-200/C. Therefore, more defect points on the surface of PtP_a/C, is one possibility leading to the higher catalytic activity of PtP_a/C to that of PtP-100/C and PtP-200/C[46].

In addition, the electronic effect on Pt is another factor that may influence catalytic methanol oxidation activity. Among the four catalysts, the change of the electronic effect between Pt and P altered the 4f electron density of Pt. From PtP_a/C to PtP-400/C, the BEs of Pt 4f XPS shifts negatively, in other words, the 4f electron density of Pt increases. Then, adsorption energy towards CO increase gradually from PtP_a/C to PtP-400/C, aiding the adsorption of CO and subsequent low catalytic methanol oxidation activity.

Fig. 10 The chronoamperometry curves normalized to Pt loading and $ECSA_{CO}$ for the four catalysts in 0.5 mol L^{-1} H$_2$SO$_4$ + 0.5 mol L^{-1} CH$_3$OH at a constant potential of 0.6 V; The inset in Figure a and b is the enlarged range between 820 and 1000 s.

Fig. 10 shows the chronoamperometry curves normalized to the Pt loading and $ECSA_{CO}$ for the four catalysts in 0.5 mol L^{-1} H$_2$SO$_4$ + 0.5 mol L^{-1} CH$_3$OH at a constant potential of 0.6 V. The potentiostatic current decreased rapidly in the initial period for the four catalysts. This was due to the formation of CO_{ads} and other intermediate species formed during the methanol

oxidation reaction. The current density gradually decayed with time and a pseudo-steady state was achieved. This decay is attributed to adsorbed intermediates such as CO on the surface of the catalyst, which can restrict methanol oxidation activity.[47] The currents of the four catalysts between 820 and 1000 s are shown in the insets. The results show that the PtP_a/C has the best durability among all the catalysts, which is consistent with the CO stripping results.

All the above electrochemical results show that the PtP_a/C electrode has a higher activity for methanol and CO oxidation than other catatlysts. The higher activity results from the combination of two factors, namely, 1) more active sites formed on the amorphous PtP_a nanoparticles due to the defect sites; 2) the electronic effect in the amorphous structure result in low adsorption energy towards CO, leading to the easy desorption of CO and further to high catalytic activity and durability.

Conclusions

In this study, XRD, TEM, line-scan EDS and XPS characterizations were used to study the effect of heat treatment temperatures on Pt-P/C catalyst structure in relation to catalyst activity. Increased temperatures changed the PtP nanoparticle structure progressively from amorphous to crystalline. At all tested temperatures, PtP nanoparticles uniformly dispersed on the carbon surface. From PtP_a/C to PtP-200/C, decrease of catalytic methanol oxidation activity coincided with less point defects and dislocation of active sites in the nanoparticles. Decreasing catalytic activities from PtP-200/C to PtP-400/C for methanol oxidation coincided with increased particle size. The CO tolerance of these catalysts corelated to the electronic structure evaluated by XPS. PtP_a/C had the higher catalytic methanol oxidation activity and strongest tolerance for CO due to both its small particle size and the amorphous structure.

Acknowledgements

Notes and references

[a]Key Laboratory of Eco-Environment-Related Polymer Materials, Ministry of Education of China, College of Chemistry and Chemical Engineering, Northwest Normal University, Lanzhou 730070, China. Fax/Tel.: +86 931 7971533; E-mail: wrf38745779@126.com, wangrf@nwnu.edu.cn.
[b]Department of Chemical Engineering, Huizhou University, Huizhou, Guangdong 516007, China
[c]South African Institute for Advanced Materials Chemistry, University of the Western Cape, Cape Town 7535, South Africa. Fax/Tel.: +27 21 9599316; E-mail: sji@uwc.ac.za

† Electronic Supplementary Information (ESI) available: the electrochemical performance of PtP-100/C. See DOI: 10.1039/b000000x/
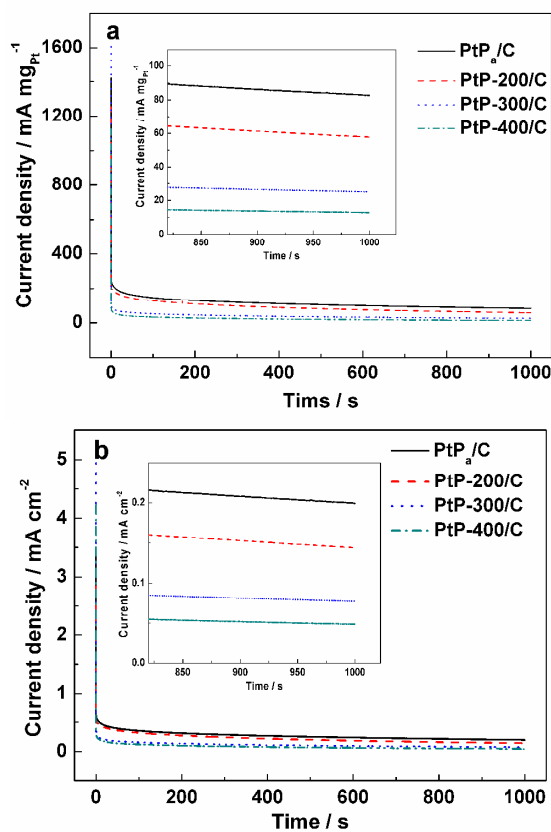
1   Y. B. He, G. R. Li, Z. L. Wang, Y. N. Ou and Y. X. Tnag, *J. Phys. Chem. C*, 2010, **114**, 19175.

2   Y. Ma, R. Wang, H. Wang and S. Ji, *Int. J. Electrochem. Sci.*, 2013, **8**, 6085.

3   A.-X. Yin, X. Q. Min, Y. W. Zhang and C. H. Yan, *J. Am. Chem. Soc.*, 2011, **133**, 3816.

4   B. Y. Xia, H. B. Wu, X. Wang and X. W. Lou, *J. Am. Chem. Soc.*, 2012, **134**, 13934.

5   C. K. Rhee, B. J. Kim, C. Ham, Y. J. Kim, K. Song and K. Kwom, *Langmuir*, 2009, **25**, 7140.

6   L. Gan, H.-D. Du, B.-H. Li, and F.-Y. Kang, *New Carbon Mater.*, 2010, **25**, 53.

7   W. Chrzanowski and A. Wieckowski, *Langmuir*, 1998, **14**, 1967.

8   P. Ferrin and M. Mavrikakis, *J. Am. Chem. Soc.*, 2009, **131**, 14381.

9   Z. Quan, Y. Wang and J. Fang, *Acc. Chem. Res.*, 2013, **46**, 191.

10 N. Tian, Z.-Y. Zhou and S.-G. Sun, *J. Phys. Chem. C*, 2008, **112**, 19801.

11 W. Y. Wong, W. R. W. Daud, A. B. Mohamad, A. A. H. Kadhum, K. S. Loh and E. H. Majlan, *Int. J. Hydrogen Energy*, 2013, **38**, 9370.

12 M. Wen, H. Liu, F. Zhang, Y. Zhu, D. Liu, Y. Tian and Q. Wu, *Chem. Commun.*, 2009, 4530.

13 O. N. Senkov and J. M. Scott, *Scripta Mater.*, 2004, **50**, 449.

14 Á. Molnár, *Appl. Surf. Sci.*, 2011, **257**, 8151.

15 K. Hashimoto, *Appl. Surf. Sci.*, 2011, **257**, 8141.

16 Z. Zhu, J. Ma, L. Xu, L. Xu, H. Li and H. Li, *ACS Catal.*, 2012, **2**, 2119.

17 D. G. Tong, W. Chu, P. Wu, G. F. Gu and L. Zhang, *J. Mater. Chem. A*, 2013, **1**, 358.

18 Y. W. Chen and D. S. Lee, *Catal. Surv. Asia*, 2012, **16**, 198.

19 S. Xie, M. Qiao, W. Zhou, G. Luo, H. He, K. Fan, T. Zhao and W. Yuan, *J. Phys. Chem. B*, 2005, **109**, 24361.

20 J. H. Byeon and Y. W. Kim, *ACS Appl. Mater. Interfaces*, 2011, **3**, 2912.

21 J. Xie and D. G. Xia, *Fuel Cells*, 2013, **13**, 143.

22 H. Wang, H. Da, S. Ji, S. Liao and R. Wang, *J. Electrochem. Soc.*, 2013, **160**, H266.

23 H. Wang, X. Zhang, R. Wang, S. Ji, W. Wang, Q. Wang and Z. Lei, *J. Power Sources*, 2011, **196**, 8000.

24 H. Wang, S. Ji, W. Wang and R. Wang, *S. Afr. J. Chem.*, 2013, **66**, 17.

25 C. Nethravathi, E. A. Anumol, M. Rajamathi and N. Ravishankar, *Nanoscale*, 2011, **3**, 569.

26 H. Peng, Z. Mo, S. Liao, H. Liang, L. Yang, F. Luo, H. Song, Y. Zhong and B. Zhang, *Sci. Rep.*, 2013, **3**.

27 L. Zhang, Y. Tang, J. Bao, T. Lu and C. Li, *J. Power Sources*, 2006, **162**, 177.

28 L. Li, L. L. Wang, D. D. Johnson, Z. Zhang, S. I. Sanchez, J. H. Kang, R. G. Nuzzo, Q. Wang, A. I. Frenkel, J. Li, J. Ciston, E. A. Stach and J. C. Yang, *J. Am. Chem. Soc.*, 2013, **135**, 13062.

29 F. Zheng, G. Mu, Z. Zhang, Y. Shen, M. Zhao and G. Pang, *Mater. Lett.*, 2012, **68**, 453.

30 L. Cheng, Z. Zhang, W. Niu, G. Xu and L. Zhu, *J. Power Source*, 2008, **182**, 91.

31 G. Yang, Y. Chen, Y. Zhou, Y. Tang and T. Lu, *Electrochem. Commun.*, 2010, **12**, 492.

32 Z. Qi and W. Lee, *Tribology International.*, 2010, **43**, 810.

33 H. Ma, J. Li, H. Chen, G. Zuo, Y. Yu, T. Ren and Y. Zhao, *Tribology International*, 2009, **42**, 940.

34 L. Castro, R. Dedryvere, M. El Khalifi, P.-E. Lippens, J. Breger, C. Tessier and D. Gonbeau, *J. Phys. Chem. C*, 2010, **114**, 17995.

35 T. C. Hufnagel, *Nat. Mater.*, 2004, **3**, 666.

36 H. W. Sheng, W. K. Luo, F. M. Alamgir, J. M. Bai and E. Ma, *Nature*, 2006, **439**, 419.

37 C. Massobrio and A. Pasquarello, *Phys. Rev. B*, 2008, **77**, 144207.

38 J. Prabhuram, T. S. Zhao, Z. K. Tang, R. Chen and Z. X. Liang, *J. Phys. Chem. B*, 2006, **110**, 5245.

39 X. T. Zhang, H. Wang, J. L. Key, V. Linkov, S. Ji, X. L. Wang, Z. Q. Lei and R. F. Wang, *J. Electrochem. Soc.*, 2012, **159**, B270.

40 H. A. Gasteiger, N. Markovic, P. N. Ross and E. J. Cairns, *J. Phys. Chem.*, 1993, **97**, 12020.

41 C. Zhou, H. Wang, F. Peng, J. Liang, H. Yu and J. Yang, *Langmuir*, 2009, **25**, 7711.

42 H. Li, G. Sun, N. Li, S. Sun, D. Su and Q. Xin, *J. Phys. Chem. C*, 2007, **111**, 5605.

43 F. Maillard, S. Schreier, M. Hanzlik, E. R. Savinova, S. Weinkaufb and U. Stimminga, *Phys. Chem. Chem. Phys.*, 2005, **7**, 385.

44 Y. Kang, X. Ye, J. Chen, L. Qi, R. E. Diaz, V. Doan-Nguyen, G. Xing, C. R. Kagan, J. Li, R. J. Gorte and E. A. Stach, *J. Am. Chem. Soc.*, 2013, **135**, 1499.

45 Y. Kang, X. Ye, J. Chen, Y. Cai, R. E. Diaz, R. R. Adzic, E. A. Stach and C. B. Murray, *J. Am. Chem. Soc.*, 2013, **135**, 42.

46 Y. Ma, R. Wang, H. Wang, V. Linkov and S. Ji, *Phys. Chem. Chem. Phys.*, 2014, **16**, 3593.

47 Y. Ma, R. Wang, H. Wang, S. Liao, J. Key, V. Linkov and S. Ji, *Materials*, 2013, **6**, 1621.

Graphical Abstract

Synthesis of ultrafine amorphous PtP nanoparticles and the effect of PtP crystallinity on methanol oxidation

Yanjiao Ma,[a] Hui Wang,[a] Hao Li,[b] Julian Key,[c] Shan Ji,[b] and Rongfang Wang,*[a]**

Ultrafine amorphous PtP nanoparticles supported on carbon black were prepared. Comparison of electrocatalytic performance of the samples with different levels of crystallinity showed ultrafine amorphous PtP nanoparticles have high catalytic activity for methanol oxidation due to its small particle size and amorphous structure.